Fully nonlinear mode competitions of nearly bicritical spiral or Taylor vortices in Taylor-Couette flow

K. Deguchi[1,*] and S. Altmeyer[2,†]

[1]*Department of Aeronautics and Astronautics, Graduate School of Engineering, Kyoto University, Yoshida-Honmachi, Sakyo-ku, Kyoto 606-8501, Japan*
[2]*Department of Mathematics, Kyungpook National University, Daegu 702-701, Korea*

Interactions between nearly bicritical modes in Taylor-Couette flow, which have been concerned with the framework of weakly nonlinear theory, are extended to fully nonlinear Navier-Stokes computation. For this purpose, a standard Newton solver for axially periodic flows is generalized to compute any mixed solutions having up to two phases, which typically arise from interactions of two spiral or Taylor vortex modes. Also, a simple theory is developed in order to classify the mixed solutions. With these methods, we elucidate pattern formation phenomena, which have been observed in a Taylor-Couette flow experiment. Focusing on the counter-rotating parameter range, all possible classes of interaction of various solutions with different azimuthal and axial wave numbers are considered within our computational restriction, and we observe numerous connection branches, e.g., footbridge solutions. Some of the mixed solutions result in a three-dimensional wavy spiral solution with axial relative periodicity or an axially doubly periodic toroidally closed vortex solution. The possible connection of the former solution family to spiral turbulence, which has been observed in highly counter-rotating Taylor-Couette flow, is discussed.

I. INTRODUCTION

TheTaylor-Couette system, consisting of a fluid between two concentric independently rotating cylinders, is one of the most famous references for pattern forming systems. Numerous structures with different topologies are known to appear in this system and have been studied extensively during the past decades.

These studies were developed in the famous paper of Andereck *et al.* [1]. As inner cylinder speed is increased, according to their experimental results, either the rotationally axisymmetric Taylor vortex flow (TVF) with toroidally closed vortices or the degenerate spiral vortex flows (SPIs) with open helicoidal left- and right-winding vortices emerge depending roughly on whether the cylinders are corotating or counter-rotating as excellently predicted by linear stability analysis of the basic state referred to as circular Couette flow (CCF).

Both of the first emerged patterns have two-dimensional structures since only a single linear unstable two-dimensional mode of the CCF grows at first. However, as inner cylinder speed is further increased, stable TVF and SPI structures are destabilized sooner by other modes resulting in the emergence of rich three-dimensional patterns.

Such mode competitions have been intensively examined in the 1960–1980s by normal form reduction of Navier-Stokes equations under the assumption of weak nonlinearity. These studies mainly concern interactions of the TVF and SPI at their bicritical points where both TVF and SPI states are linearly critical so that the nonlinearity of the resultant mixed modes is weak. Albeit the restriction, the reduced problem successfully explains qualitative bifurcation scenarios of mixed solution branches. Detailed theoretical descriptions of the weakly nonlinear analysis and comparisons to experimental results are well documented in Refs. [2–6]. As a result, various three-dimensional vortex states with sinusoidal azimuthal variation, such as wavy vortex flow (WVF), twisted vortex flow (TWI), wavy inflow boundaries (WIBs), and wavy outflow boundaries (WOBs), defined in terms of a flat or wavy vortex cell boundary, have been found. These structures have also been identified in experiments (e.g., Refs. [1,7,8]) and fully nonlinear computations via three-dimensional Floquet instability of the TVF (e.g., Refs. [9,10]).

Another type of mode competition has been found in an interaction between oppositely traveling right- and left-winding SPI modes, which are mirror images of each other. As can be seen from its construction, the mixed state, called a ribbon (RIB), has a common bifurcation point as the two SPI solutions, presenting an axially standing-wave structure [11]. This nonlinear SPI superposition is recently extended to cross spirals with different amplitudes [12] and pitches [13]. In Refs. [12,13], stable and unstable equilibrated wavy spiral patterns (WSPs) were observed simulating Navier-Stokes equations in carefully chosen symmetry restricted subspaces with axially periodic constraints. A similar pattern has also been observed in transitions between SPI and TVF [14], which had theoretically been predicted by weakly nonlinear theory [4,5].

Although three-dimensional finite-amplitude solutions of Navier-Stokes equations in the Taylor-Couette flow have been studied by simulation or Floquet stability theory to the TVF as above for some time, corresponding bifurcation analysis near bicritical points is intensively examined here, since one of our motivations is to bridge the bicritical bifurcation scenario by weakly nonlinear analysis and fully nonlinear computation of finite-amplitude solutions. Another motivation comes from the fact that, in all weakly and fully nonlinear calculations, so far, the wave numbers of superimposed states are chosen

to be identical so that the resultant mixed state also has the same axial periodicity. Thus, we extend the standard numerical method in order to compute interaction analysis for the general axial wave number choice. To find the possible symmetry of the bifurcating mixed solution branches in the general situation, we also propose a simplified theoretical approach considering the form of the solutions' phases instead of the normal form reduction or formal group theory, which makes arguments more complex.

There is also a large physical interest in the general axial wave number case. It has been shown by Refs. [15–19] that, for highly counter-rotating Taylor-Couette flow, an axially large structure due to an inclined and banded spatially intermittent pattern emerges. For such a situation, the relative periodicity in an axial direction, i.e., flow fields at upper and lower lids coincide when a proper azimuthal shift is applied, is considered to be a more suitable choice of boundary conditions than the usual axial periodic conditions. Our interaction analysis, indeed, yields this condition as a result. With this application in mind, the parameter range is adjusted to that of Ref. [18] throughout the paper.

The paper is subdivided into five main parts. Following the introduction, Sec. II describes the mathematical formulation of the problem. We describe our numerical method based on Newton's iterative method since, as found in Ref. [20], some solution branches can be weakly subcritical in counter-rotating Taylor-Couette flow. In Sec. III, we begin with the analysis of the system by examining the possible symmetry of mixed solutions. Based on the symmetry analysis, Sec. IV presents the Navier-Stokes computational results of various nonlinearly interacting equilibrated solutions. Finally, we discuss our results and draw some conclusions in Sec. V.

II. FORMULATION OF THE PROBLEM

A. Governing equations

We consider a fluid flow driven in an annular gap between two infinitely long independently rotating cylinders. The inner cylinder of radius r_i^* rotates with angular speed Ω_i^*, and the outer cylinder of radius r_o^* rotates with angular speed Ω_o^*. The fluid in the annulus is considered to be Newtonian, isothermal, and incompressible with kinematic viscosity ν^* and density ρ^*. Using the gap width $d^* = r_o^* - r_i^*$, the radial diffusion time d^{*2}/ν^*, and ρ^* as the length, time, and density scales, respectively, the velocity in cylindrical coordinates $(r,\theta,z), \mathbf{u} = u\mathbf{e}_r + v\mathbf{e}_\theta + w\mathbf{e}_z$, and pressure p are governed by the nondimensional Navier-Stokes and continuity equations,

$$\partial_t \mathbf{u} + (\mathbf{u} \cdot \nabla)\mathbf{u} = -\nabla p + \nabla^2 \mathbf{u}, \quad \nabla \cdot \mathbf{u} = 0, \quad (1)$$

together with no-slip conditions on the cylinder walls. The system has three parameters: the inner Reynolds number $\mathrm{Re}_i = \Omega_i^* r_i^* d^*/\nu^*$, the outer Reynolds number $\mathrm{Re}_o = \Omega_o^* r_o^* d^*/\nu^*$, and the radius ratio $\eta = r_i^*/r_o^*$. Both latter parameters are fixed in this paper with $\mathrm{Re}_o = -1200$ and $\eta = 0.883$, which are used in Meseguer *et al.* [18,20]. The basic solution of the system is given by the circular Couette flow (CCF) profile,

$$\mathbf{u}_{\mathrm{CCF}}(r) = v_{\mathrm{CCF}}(r)\mathbf{e}_\theta = \{Ar + Br^{-1}\}\mathbf{e}_\theta, \quad (2)$$

where the no-slip boundary conditions determine the coefficients $A = \frac{\mathrm{Re}_o - \eta\,\mathrm{Re}_i}{1+\eta}$ and $B = \frac{\eta(\mathrm{Re}_i - \eta\,\mathrm{Re}_o)}{(1-\eta)^2(1+\eta)}$.

Considering periodic or relative periodic boundary conditions in the axial direction, i.e., the flow field satisfies $\mathbf{u}(r,\theta,z,t) = \mathbf{u}(r,\theta + \epsilon, z + \delta, t)$, for some $\epsilon, \delta \in \mathbb{R}$, the governing equations Eq. (1) and the boundary conditions are invariant under rotations $R_{\theta'}$ with arbitrary angle θ' about the cylinder axis, axial translations $T_{z'}$, time translations $\Phi_{t'}$, and reflection σ about $z = 0$ at arbitrary height. The actions of these symmetries on velocities and pressure are

$$R_{\theta'}(u,v,w,p)(r,\theta,z,t) = (u,v,w,p)(r,\theta + \theta',z,t), \quad (3a)$$

$$T_{z'}(u,v,w,p)(r,\theta,z,t) = (u,v,w,p)(r,\theta,z + z',t), \quad (3b)$$

$$\Phi_{t'}(u,v,w,p)(r,\theta,z,t) = (u,v,w,p)(r,\theta,z,t + t'), \quad (3c)$$

$$\sigma(u,v,w,p)(r,\theta,z,t) = (u,v,-w,p)(r,\theta,-z,t). \quad (3d)$$

B. Numerical methods

The numerical scheme throughout the present paper is based on Ref. [21], which solves the three-dimensional traveling-wave solutions of Eq. (1) in a rectangular periodic domain $(\theta,z) \in [0,2\pi/n_0] \times [0,2\pi/k_0]$, where n_0 and k_0 represent the azimuthal and axial wave numbers, respectively. We first briefly summarize this method and then proceed to the more complicated present case.

The key methodology used in Ref. [21] is the multidimensional Newton-Raphson iterative scheme for the quadratic algebraic equations $F_i = D_{ij} X_j + H_{ijj'} X_j X_{j'} = 0$, which is obtained as a result of Fourier-Galerkin and Chebyshev-collocation discretization of the governing equations (1) introducing the potential approach [22] where the velocities are decomposed as $\mathbf{u} = \overline{v}\mathbf{e}_\theta + \overline{w}\mathbf{e}_z + \nabla \times \nabla \times (\phi\mathbf{e}_r) + \nabla \times (\psi\mathbf{e}_r)$. Potentials ϕ and ψ and mean flows $\overline{v}$ and $\overline{w}$, which are defined by the θ-z average over the periodic domain, are approximated as

$$\phi(r,\varphi_1,\varphi_2) = \sum_{l=0}^{L} \sum_{\substack{n=-N \\ (n,k)\neq(0,0)}}^{N} \sum_{k=-K}^{K} X_{lnk}^{(1)} f_l(x) e^{i(n\varphi_1 + k\varphi_2)}, \quad (4)$$

$$\psi(r,\varphi_1,\varphi_2) = \sum_{l=0}^{L} \sum_{\substack{n=-N \\ (n,k)\neq(0,0)}}^{N} \sum_{k=-K}^{K} X_{lnk}^{(2)} g_l(x) e^{i(n\varphi_1 + k\varphi_2)}, \quad (5)$$

$$\overline{v}(r) = v_{\mathrm{CCF}}(r) + \sum_{l=0}^{L} X_{l00}^{(1)} g_l(x), \quad (6)$$

$$\overline{w}(r) = \sum_{l=0}^{L} X_{l00}^{(2)} g_l(x), \quad (7)$$

where $f_l(x) = (1-x^2)^2 T_l(x)$ and $g_l(x) = (1-x^2) T_l(x)$ are the modified lth Chebyshev polynomials T_l. In order to use Chebyshev expansion, the radial coordinate is mapped to $x = 2(r - r_m) \in [-1,1]$ by using mean radius $r_m = (r_i + r_o)/2$. The rest of the variables can be summarized in two phases φ_1 and φ_2. For three-dimensional traveling waves in the rectangular periodic domain, the phases are $[\varphi_1,\varphi_2] = [n_0(\theta - C_\theta t), k_0(z - C_z t)]$, denoting the azimuthal and axial phase speeds as C_θ and C_z, respectively. In the following, it will be found that this expression is just a special case of the methodology throughout the paper.

Here, the present computational approach considers the more general situation: We assume that the solution of Eq. (1)

can be written in r and the generalized two phases,

$$[\varphi_1, \varphi_2] = [a_1\theta + b_1 z - c_1 t, a_2\theta + b_2 z - c_2 t], \quad (8)$$

where $a_1, a_2, b_1,$ and b_2 are the generalized wave numbers and c_1 and c_2 are the generalized frequencies (note that, physically, a_1 and a_2 must be integers to assure 2π azimuthal periodicity, although there is no mathematical and computational inconveniences when they are noninteger values). With this generalization, we can consider a wider class of solutions than the previous method. The equations to be solved for this general case can easily be obtained from the previous formulation by replacing $[\theta, z, t]$ derivative operators $inn_0, ikk_0,$ and $-i(nn_0 C_\theta + kk_0 C_z)$ with $in(a_1 + a_2), ik(b_1 + b_2),$ and $-i(nc_1 + kc_2),$ respectively. If all of the wave numbers $a_1, a_2, b_1,$ and b_2 are nonzero, the flow regime is periodic in a parallelogram shape domain in an unrolled θ-z plane, spanned by two vectors $[\theta, z] = [\theta', z']$ and $[\theta'', z'']$ (cf. Fig. 1). The values of these vectors can be obtained as

$$[\theta', z'] = \left[\frac{2\pi b_2}{a_1 b_2 - a_2 b_1}, \frac{-2\pi a_2}{a_1 b_2 - a_2 b_1} \right], \quad (9)$$

and

$$[\theta'', z''] = \left[\frac{-2\pi b_1}{a_1 b_2 - a_2 b_1}, \frac{2\pi a_1}{a_1 b_2 - a_2 b_1} \right], \quad (10)$$

by solving $[2\pi, 0] = [a_1\theta' + b_1 z', a_2\theta' + b_2 z']$ and $[0, 2\pi] = [a_1\theta'' + b_1 z'', a_2\theta'' + b_2 z'']$. The phase speeds in the $[\theta', z']$ and $[\theta'', z'']$ directions are

$$C' = \frac{c_1\sqrt{a_2^2 + b_2^2}}{a_1 b_2 - b_1 a_2}, \quad (11)$$

and

$$C'' = \frac{c_2\sqrt{a_1^2 + b_1^2}}{a_1 b_2 - b_1 a_2}, \quad (12)$$

respectively. By setting $N = 0$ or $K = 0$ in Eqs. (4) and (5), we can compute the solution, which has only one phase. In this case, one phase-lock condition is needed.

Here, we want to remark that, for $(a_1, a_2, b_1, b_2) = (n_0, 0, 0, k_0)$, we recover the formulation of Ref. [21], described above. Notice also that the unknown vector X_i in the algebraic equations includes the phase speeds in addition to the spectral coefficients. Additional equations for them are phase-lock conditions for φ_1 and φ_2 [e.g., $\mathrm{Im}(X_{120}^{(1)}) = \mathrm{Im}(X_{102}^{(1)}) = 0$].

As a quantity to measure different finite-amplitude solutions, we use the CCF-normalized torque on the inner cylinder wall Δ, given by

$$\Delta = \left. \frac{-r^3 \partial_r (r^{-1}\overline{v})}{-r^3 \partial_r (r^{-1} v_{\mathrm{CCF}})} \right|_{r=r_i}. \quad (13)$$

III. PHASE SYMMETRY ANALYSIS

The aim of this section is the classification of solutions in terms of the form of their phases and symmetry. Although the solution $\mathbf{X} \in (u, v, w, p, c_1, c_2)$ is considered to have two phases in the following preliminary, the argument is the same if the number of phases is different.

A general problem which arises when we consider the symmetry of solutions is that, even when a solution is invariant under some operation $\mathcal{S}$, sometimes this property is not preserved when the origin of the $[\theta, z, t]$ coordinate is changed. Therefore, for the sake of simplicity, we say solution $\mathbf{X}$ is *essentially invariant* to operator $\mathcal{S}$ if there exist $\theta', z', t' \in \mathbb{R}$ such that $\mathcal{S} R_{\theta'} T_{z'} \Phi_{t'} \mathbf{X} = R_{\theta'} T_{z'} \Phi_{t'} \mathbf{X}$. We pose two assumptions in the symmetry analysis.

(i) The first assumption is that $\mathbf{X}$ is periodic in φ_1 and φ_2 with fundamental period 2π, namely,

$$\tau_{\delta_1, \delta_2} \mathbf{X} = \mathbf{X} \Leftrightarrow \delta_1, \quad \delta_2 \in \mathbb{Z}, \quad (14)$$

where the translation operator for the phases is defined as

$$\tau_{\delta_1, \delta_2} \mathbf{X}(r, \varphi_1, \varphi_2) = \mathbf{X}(r, \varphi_1 + 2\pi\delta_1, \varphi_2 + 2\pi\delta_2), \quad (15)$$

where "$\Leftrightarrow$" means the left and right statements are logically equivalent. This condition ensures every pattern to be unique in a fundamental periodic cell, i.e., $(\varphi_1, \varphi_2) \in [0, 2\pi] \times [0, 2\pi]$. The time and spatial shift operation $R_{\theta'} T_{z'} \Phi_{t'}$ is identical to the phase shift operation $\tau_{\delta_1, \delta_2}$ if $[2\pi\delta_1, 2\pi\delta_2] = [a_1\theta' + b_1 z' - c_1 t', a_2\theta' + b_2 z' - c_2 t']$ is satisfied. Therefore, we can also consider the symmetry of solutions in terms of phases ($\mathbf{X}$ is essentially invariant to $\mathcal{S}$ if there exist $\delta_1, \delta_2 \in \mathbb{R}$ such that $\mathcal{S}\tau_{\delta_1, \delta_2} \mathbf{X} = \tau_{\delta_1, \delta_2} \mathbf{X}$).

(ii) The second assumption is that the operator $\mathcal{S}$ is an arbitrary combination of some $R_{\theta'_i}, T_{z'_i}, \Phi_{t'_i},$ and σ where $\theta'_i, z'_i, t'_i \in \mathbb{R}$ for $i = 1, 2, \ldots$. Note that such a $\mathcal{S}$ can be rewritten in either $\tau_{\epsilon_1, \epsilon_2}$ or $\tau_{\epsilon_1, \epsilon_2}\sigma$ by using some $\epsilon_1, \epsilon_2 \in \mathbb{R}$. Note that, for the former case, $\epsilon_1, \epsilon_2 \in \mathbb{Z}$ by assumption (14), and there is no special case. Thus, in the following subsections, we list all possible symmetries of one- and two-phase solutions restricting attention to the latter case.

A. One phase

Suppose $\mathbf{X}(r, \varphi_1)$ is essentially invariant to $\mathcal{S} = \tau_{\epsilon_1}\sigma$ where the translation operator is defined by

$$\tau_{\delta_1} \mathbf{X}(r, \varphi_1) = \mathbf{X}(r, \varphi_1 + 2\pi\delta_1). \quad (16)$$

The dependence of the phase against reflectional operation σ determines the symmetry of the solution. Since $\mathcal{S}$ acts on the phases as a linear operator which does not break the form of the phases, simple analysis of an equation $\sigma\varphi_1 = \Sigma\varphi_1$, where $\Sigma \in \mathbb{R}$, yields all possible cases. Recalling that σ is the reflectional operator which does not change the length unit of the phase, Σ must be either 1 or -1. Note that this is consistent with the fact that by twice considering the operations of σ, we find the identity.

(1) If $\sigma\varphi_1 = \varphi_1$, then $\varphi_1 = a_1\theta - c_1 t$. The solution satisfies $\sigma\mathbf{X} = \mathbf{X}$, and the operators τ_{δ_1} and σ are commutative ($\tau_{\delta_1}\sigma = \sigma\tau_{\delta_1}$) for any $\delta_1 \in \mathbb{R}$. It will be shown that this type of instability is absent in our considered parameter region. However, here, we remark that this type of solution is called the *Tollmien-Schlichting wave* in the boundary-layer or channel-flow problem. Using assumption (14), we find the shift value ϵ_1 in the operation $\mathcal{S}$ belongs to $\mathbb{Z}$.

(2) If $\sigma\varphi_1 = -\varphi_1$, then $\varphi_1 = b_1 z$. The operators τ_{δ_1} and σ are anticommutative ($\tau_{\delta_1}\sigma = \sigma\tau_{-\delta_1}$) for any $\delta_1 \in \mathbb{R}$. We call this type of solution the *Taylor vortex flow* (TVF).

Note that, for any ϵ_1 (**X** is essentially invariant to $\mathcal{S}$) $\Leftrightarrow$ (**X** is essentially invariant to σ).

(3) If **X** is not essentially invariant to $\mathcal{S}$, then $b_1 \neq 0$. The solution **X** is called the *spiral vortex flow* (SPI). As a result of symmetry breaking, there exist degenerate left- and right-winding SPI solutions which satisfy cross parity against $\mathcal{S}$ [the result of operation $\mathcal{S}$ to a left-winding (right-winding) SPI solution is a right-winding (left-winding) SPI solution]. Note that this case also includes traveling-wave type Taylor vortex flows with a phase $\varphi_1 = b_1 z - c_1 t$.

B. Two phases

Suppose $\mathbf{X}(r, \varphi_1, \varphi_2)$ is essentially invariant to $\mathcal{S} = \tau_{\epsilon_1, \epsilon_2} \sigma$. To extract all possible symmetries, consider an equation $\sigma[\varphi_1, \varphi_2] = \Sigma[\varphi_1, \varphi_2]$, where $\Sigma \in \mathbb{R}^{2 \times 2}$. The matrix Σ must have two 1 or -1 components and two zero components (since the result of the operation must also have two phases). By twice considering the operations of σ, we find Σ^2 must be an identity matrix. Such a matrix is either

$$\begin{bmatrix} I & 0 \\ 0 & J \end{bmatrix} \quad \text{or} \quad \begin{bmatrix} 0 & I \\ I & 0 \end{bmatrix} \quad \text{with} \quad I, J \in \{1, -1\}. \quad (17)$$

(1) If $\sigma[\varphi_1, \varphi_2] = [\varphi_1, \varphi_2]$, then $[\varphi_1, \varphi_2] = [a_1 \theta - c_1 t, a_2 \theta - c_2 t]$. The *doubly periodic Tollmien-Schlichting wave* solution found by Ref. [23] in channel flow is this type, but it is not possible to identify similar solutions in our model and parameter range. In this case, $\sigma \mathbf{X} = \mathbf{X}$ is satisfied. Together with the relation $\tau_{\delta_1, \delta_2} \sigma = \sigma \tau_{\delta_1, \delta_2}$, for any $\delta_1, \delta_2 \in \mathbb{R}$, one finds the shift values ϵ_1, ϵ_2 in the operation $\mathcal{S}$ belong to $\mathbb{Z}$.

(2) If $\sigma[\varphi_1, \varphi_2] = [-\varphi_1, -\varphi_2]$, then $[\varphi_1, \varphi_2] = [b_1 z, b_2 z]$. We call this type of solution the *doubly periodic Taylor vortex flow* (dTVF). Since $\tau_{\delta_1, \delta_2} \sigma = \sigma \tau_{-\delta_1, -\delta_2}$ for any $\delta_1, \delta_2 \in \mathbb{R}$ (**X** is essentially invariant to $\mathcal{S}$) $\Leftrightarrow$ (**X** is essentially invariant to σ) for any $\epsilon_1, \epsilon_2 \in \mathbb{R}$. Note that, if $b_1/b_2 \in \mathbb{Z}$, i.e., the wave numbers of the phases are rational, **X** can be rewritten in only one phase $\varphi_1 = b_1 x$ and, thus, reduces to TVF.

(3) If $\sigma[\varphi_1, \varphi_2] = [\varphi_1, -\varphi_2]$, then $[\varphi_1, \varphi_2] = [a_1 \theta - c_1 t, b_2 z]$, i.e., the solution is a three-dimensional traveling wave (the case $\sigma[\varphi_1, \varphi_2] = [\varphi_1, -\varphi_2]$, i.e., $[\varphi_1, \varphi_2] = [b_1 z, a_2 \theta - c_2 t]$, leads to a similar argument). The relation $\tau_{\delta_1, \delta_2} \sigma = \sigma \tau_{\delta_1, -\delta_2}$ holds for any $\delta_1, \delta_2 \in \mathbb{R}$. Since **X** must also essentially be invariant to $\mathcal{S}^2 = \tau_{2\epsilon_1, 0}$, the shift value ϵ_1 belongs to either $\mathbb{Z}$ or $\mathbb{Z} + 1/2$ and (**X** is essentially invariant to $\mathcal{S}$) $\Leftrightarrow$ (**X** is essentially invariant to σ), for any $\epsilon_2 \in \mathbb{R}$ (therefore, the shift value ϵ_2 is set out to 0 in the following), is satisfied. This implies there are three possible cases.

(i) **X** is essentially invariant to the so-called *reflection symmetry* σ but not essentially invariant to the so-called *shift-reflection symmetry* $\tau_{1/2, 0} \sigma$. We call this type of solution the *twisted vortex flow* (TWI).

(ii) **X** is essentially invariant to shift-reflection symmetry $\tau_{1/2, 0} \sigma$ but not essentially invariant to reflection symmetry σ. We call this type of solution the *wavy vortex flow* (WVF).

(iii) If **X** is essentially invariant to both reflection symmetry and shift-reflection symmetry σ and $\tau_{1/2, 0} \sigma$, then $\sigma \tau_{0, \delta_2 + \delta} \mathbf{X} = \tau_{0, \delta_2 + \delta} \mathbf{X}$, and $\tau_{1/2, 0} \sigma \tau_{0, \delta_2} \mathbf{X} = \tau_{0, \delta_2} \mathbf{X}$ holds for some $\delta, \delta_2 \in \mathbb{R}$. However, by combining these relations, we can deduce $\tau_{1/2, 2\delta} \mathbf{X} = \mathbf{X}$, which contradicts
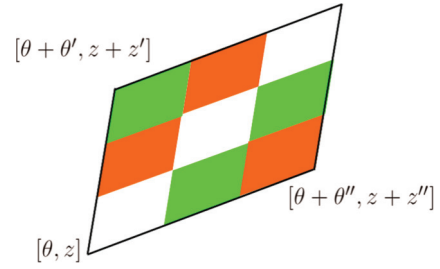

FIG. 1. (Color online) The parallelogram domain bounded by thick solid lines shows one fundamental periodic cell. The assumption (18) allows the obliquely aligned same pattern as in the colored regions, i.e., $\tau_{1/3, 1/3} \mathbf{X} = \mathbf{X}$, whereas, the assumption (14) does not.

assumption (14). In order to understand this case more clearly, it is worth changing the assumption (14) to

$$\begin{aligned} \tau_{\delta_1, 0} \mathbf{X} = \mathbf{X} &\Leftrightarrow \delta_1 \in \mathbb{Z}, \\ \tau_{0, \delta_2} \mathbf{X} = \mathbf{X} &\Leftrightarrow \delta_2 \in \mathbb{Z}. \end{aligned} \quad (18)$$

The new assumption (18) implies the restriction for the solutions is "relaxed" from (14) in some sense since it does not say anything for the multishift. Therefore, it is possible to realize the same pattern in a fundamental periodic cell as in Fig. 1. Under this new assumption, we can find $2\delta \notin \mathbb{Z}$ and $4\delta \in \mathbb{Z}$, i.e., **X** must also be essentially invariant to $\tau_{1/2, 1/2}$. Note that, by switching phases as $\varphi_1 + \varphi_2 \to \varphi_1$ and $\varphi_1 - \varphi_2 \to \varphi_2$, this case coincides with the next case, the ribbon.

(4) If $\sigma[\varphi_1, \varphi_2] = [\varphi_2, \varphi_1]$, then $[\varphi_1, \varphi_2] = [a\theta + bz - ct, a\theta - bz - ct]$ (the case of $\sigma[\varphi_1, \varphi_2] = [-\varphi_2, -\varphi_1]$, i.e., $[\varphi_1, \varphi_2] = [a\theta + bz - ct, -a\theta + bz + ct]$, leads to a similar argument). The relation $\tau_{\delta_1, \delta_2} \sigma = \sigma \tau_{\delta_2, \delta_1}$ holds for any $\delta_1, \delta_2 \in \mathbb{R}$. We call this type of solution the *ribbon* (RIB).

We note here that $\mathcal{S}$ can be transformed into $\tau_{-\epsilon_2/2, -\epsilon_1/2} \tau_{(\epsilon_1 + \epsilon_2)/2, (\epsilon_1 + \epsilon_2)/2} \sigma \tau_{\epsilon_2/2, \epsilon_1/2}$ in this case. This means (**X** is essentially invariant to $\mathcal{S}$) $\Leftrightarrow$ (**X** is essentially invariant to $\tau_{(\epsilon_1 + \epsilon_2)/2, (\epsilon_1 + \epsilon_2)/2} \sigma$). Recalling $\epsilon_1 + \epsilon_2 \in \mathbb{Z}$, we can find the solution is essentially invariant to both reflection symmetry σ and shift-reflection symmetry $\tau_{1/2, 1/2} \sigma$. The difference between the present case and (iii) in the last case is the choice of periodic cell as indicated in Figs. 2(a) and 2(b), respectively.
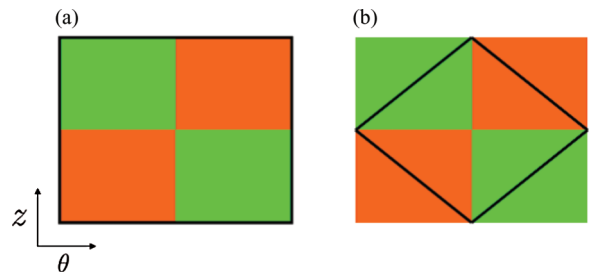

FIG. 2. (Color online) Schematics of two choices of periodic domain for RIB solutions. The thick solid lines show the boundary of a fundamental periodic cell. The regions in the same color indicate the same patterns. Note that (a) is not compatible to assumption (14), whereas, (b) satisfies both of the assumptions (14) and (18).

Note that standing-wave type Taylor vortex flows, which have phases $[\varphi_1, \varphi_2] = [bz - ct, bz + ct]$, are included in this case.

(5) If **X** is not essentially invariant to $\mathcal{S}$, then $b_1 \neq 0$ and $b_2 \neq 0$. We call this type of solution the *wavy spiral vortex flow* (WSP). Cross parity exists for this solution type due to the symmetry breaking.

As an overall remark about this section, here, we note that, so far, the flow classification has been performed only in terms of symmetry. Hence, the terminologies in this paper can differ from those used in the simulations and experiments referred to in Sec. I, despite our best efforts to maintain consistency between them.

IV. NUMERICAL RESULTS

In this section, we apply the phase symmetry analysis in the last section to the bifurcation problem of (1). We start our numerical analysis in the first subsection clarifying the linear stability properties of the basic flow against various axisymmetric and nonaxisymmetric modes in the parameter region we investigate in this paper. For some particular parameter choices, called bicritical points, two distinct critical instabilities coexist. The analysis in Sec. III yields the symmetry of possible bifurcating nonlinear solutions from the superposition of these linear bicritical modes. Therefore, we can omit weakly nonlinear analysis, which formally ensures the existence of a nonlinear mixed solution, and directly proceed to fully nonlinear computations elucidating the interactions of SPI-SPI, SPI-TVF, and TVF-TVF instabilities.

A. Linear stability of the basic flow

As a preliminary of nonlinear analysis, we examine the linear instability, i.e., the instability against infinitesimally small disturbances to the basic flow. Neglecting nonlinear terms, the solutions of the linearized problem are proportional to $\exp(in_0\theta + ik_0z + \gamma t)$ where the sign of the real part of the complex growth rate $\gamma \in \mathbb{C}$ determines whether the disturbances grow or decay. Therefore, if $n_0 \neq 0$ and $k_0 \neq 0$, the critical solutions have SPI type symmetry, in general. When some axial wave number k_0 is taken, SPI modes with an azimuthal wave number $n_0 = \pm m, m \in \mathbb{Z}$ shows the same stability property. Note that the symmetry of the system allows us to only consider positive k_0.

For the present control parameters $(\eta, \mathrm{Re}_o) = (0.883, -1200)$, Meseguer *et al.* [20] showed, as increasing Re_i, the basic flow encounters, first, SPI type instability with $n_0 = \pm 5$ at $(\mathrm{Re}_i, k_0) = (447.35, 5.125)$ and then, SPI type instability with $n_0 = \pm 4$ at $(\mathrm{Re}_i, k_0) = (470.44, 3.76)$. The red (medium gray) solid curves in Fig. 3 indicate the critical curves taken all over k_0 for these $n_0 = 5$ and $n_0 = 4$ SPI modes, respectively. For $n_0 = 0$, the critical curve is depicted as the green (light gray) solid curve. On this critical curve, we confirm that the real part of γ is identical to zero, suggesting that this mode has TVF type symmetry. The green (light gray) dot-dashed curve is essentially the same result as the solid TVF curve, but the value of k_0 is divided by a factor of 2. This means the curve represents a stability boundary for two-cell TVF within $z \in [0, 2\pi/k_0]$ (hereinafter, we abbreviate m-cell TVF states as TVF $\times m$ using $m \in \mathbb{N}$). Within the investigated
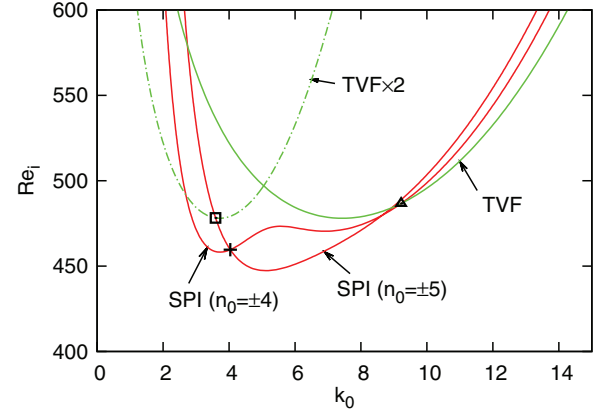

FIG. 3. (Color online) The linear critical curves for $(\eta, \mathrm{Re}_o) = (0.883, -1200)$. The SPI type stability boundaries are indicated by red (medium gray) curves, whereas, those of the TVF type are indicated by green (light gray) curves. The instabilities are examined against k_0, which is taken to be the fundamental period except for the dot-dashed curve where a two-cell state [denoted as (TVF $\times$ 2)] is considered in $z \in [0, 2\pi/k_0]$. The bicritical points of SPI instabilities with $n_0 = \pm 5$ and $n_0 = \pm 4$, a SPI instability with $n_0 = \pm 4$ and a TVF instability, and a SPI instability with $n_0 = \pm 5$ and a TVF $\times$ 2 instability are marked by a $+$, a $\triangle$, and a $\square$, respectively.

parameter region, there is no Tollmien-Schlichting wave type linear instability as remarked in Sec. III A.

B. SPI-SPI interactions

Using a linear critical disturbance as an initial guess of Newton's method, one can obtain finite-amplitude solutions of (1). The resultant solution branch bifurcating from a single SPI type linear critical disturbance must inherit SPI symmetry as observed in Ref. [20]. In this subsection, we focus on nonlinear interactions of several SPI type instabilities. In order to obtain such mixed states, we use superimposed linear critical SPI disturbances as an initial guess for Newton iterations. For the sake of simplicity, first, we consider the interactions of SPI solutions which have an equal axial wave number k_0. In this case, the story is similar to Refs. [12,13], but the approach is different here. The mixed solutions are produced in the vicinity of the bicritical point $(k_0^+, \mathrm{Re}_i^+) = (4.037, 459.62)$ where the linear critical curves of $n_0 = \pm 5$ and ± 4 intersect at the "$+$" marked in Fig. 3. The bifurcation scenarios at $k_0 < k_0^+$ and $k_0 > k_0^+$ are shown in Figs. 4(a) and 4(b), respectively. The two red (medium gray) thin curves in the figures represent the SPI solution branches. We denote SPI solutions with n_0 azimuthal dependence as S_{n_0} in this subsection. As we already remarked, left- and right-winding spirals, which have phases $(n_0\theta + k_0z - ct)$ and $(-n_0\theta + k_0z + ct)$, respectively, for $n_0 > 0$, bifurcate simultaneously at the SPI critical point (note that they are degenerate in the bifurcation diagrams). Therefore, in principle, interactions of arbitrary combinations of S_4, S_5, S_{-4}, and S_{-5} disturbances can be considered, although we only discuss the interactions of two of them due to our numerical code restriction.

Practically, mixed mode calculations can be performed by choosing the two phases φ_1 and φ_2 in Eqs. (4) and (5) as the two original SPI solution phases. These solutions are input in
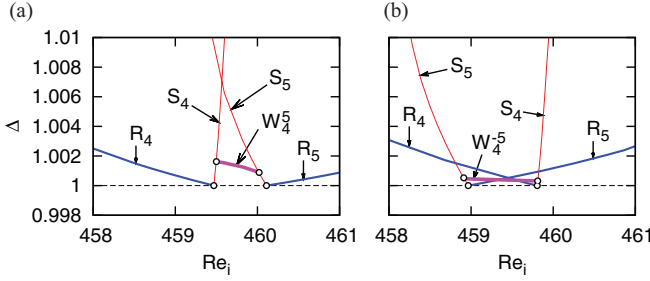
FIG. 4. (Color online) The bifurcation diagrams near the bicritical point of S^5 and S^4 disturbances $(k_0^+, \mathrm{Re}_i^+) = (4.037, 459.62)$ in Fig. 3 for (a) $k_0^+ > k_0 = 4.02$ and (b) $k_0^+ < k_0 = 4.06$. The red (medium gray) thin, blue (dark gray) medium thick, and magenta (medium gray) thick curves correspond to solutions with SPI, RIB, and WSP symmetries, respectively. Here and hereinafter, the bifurcation points in the bifurcation diagrams are indicated by open circles, and only one of the overlapped solutions (e.g., S_5 and S_{-5}) is indicated for the sake of simplicity (cf. Sec. III).

entries $X_{ln0}^{(j)}$ and $X_{l0k}^{(j)}$ multiplied by some weights to provide an initial guess of the Newton iterative scheme in the vicinity of a bicritical point. If the weights are proper, the iterations converge to a mixed solution.

The nonlinearly superimposed equilibrated solutions of the left-winding SPI solutions and their right-winding counterparts are plotted as the blue (dark gray) medium thick curves in Fig. 4. Comparing the phases and the arguments in Sec. III, one finds the mixed solutions have RIB type symmetry. Henceforth, the interaction of $S_5[S_4]$ and $S_{-5}[S_{-4}]$ is denoted by $R_5[R_4]$. Note that these RIB and SPI solutions must bifurcate from the same critical point.

In contrast, the mixed mode branch between SPI solutions with different pitches does not connect to the basic state but bridges the two SPI solution branches instead [the thick magenta (medium gray) curves in Fig. 4]. Since this type of mixed solution has WSP type symmetry, we denote the S_i-S_j bridge solution as W_j^i for short. As explained in Sec. III, W_j^i and W_{-j}^{-i} solution branches are overlapped in the bifurcation diagram. The fact that the $W_4^{-5}(W_{-4}^5)$ branch only exists if $k_0 > k_0^+$, whereas the $W_4^5(W_{-4}^{-5})$ branch only exists if $k_0 < k_0^+$, suggests the annihilation of the end points of the branches at the bicritical point (k_0^+, Re_i^+).

The W_4^{-5} solution continues to exist in a wider range of Re_i when the axial wave number is increased to $k_0 = 5.125$ (cf. Fig. 5). For this parameter, the azimuthal vorticity $\omega = \partial_z u - \partial_r w$ of typical $S_5, S_4, R_5, R_4,$ and W_4^{-5} solutions are visualized in Figs. 7(a)–7(e). All of the plots in Fig. 7 are depicted at quarter gap $r - r_m = -0.25$ in rectangular domain $(\theta, z) \in [0, 2\pi] \times [0, 2\pi/k_0]$ where the all flow regimes are periodic. The visualizations of the SPI and RIB solutions are consistent with Ref. [20], whereas, the W_4^{-5} solution has a similar appearance to Ref. [13].

The branch of W_4^5 solutions, which is the mixed state between two SPI solutions with an equal sigh of helicities reported here, can be continued for a smaller axial wave number $k_0 = 3.94$ (cf. Fig. 6). For this wave number, the bifurcation diagram looks much more complicated than Fig. 4(a). This is due to the reconnection of the W_4^5 solution
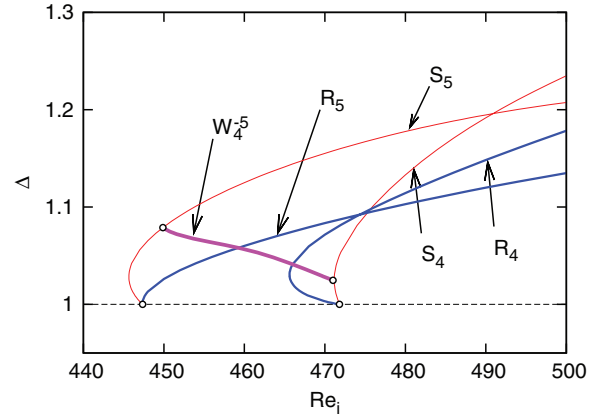
branch to another bridge solution as k_0 is decreased. As a result, two segments of solution branches, whose both end points are attached to the same SPI solution branch, emerge. This is analogous to the bypass WSP solution branches found in Ref. [13]. Another reason for the complexity is the presence of the second turning point of the RIB solution branches. After this turning point, both R_5 and R_4 solution branches connect to the TVF $\times$ 2 solution branch, which is originated from the green (light gray) dot-dashed linear critical curve in Fig. 3 (we will examine the bifurcation of the RIB solution from the TVF $\times$ 2 solution in Sec. IV C). The flow visualization of the W_4^5 solution, Fig. 7(f), shows a spiral-like dominated structure, but we can clearly see fringe due to the nonlinear interference of the S^5 and S^4 solutions.

The method is the same, even when the interacting SPI solutions have different k_0's. The exemplary Fig. 8 illustrates the bridge solution between S_{-5} with $k_0 = 5.125$ (cf. Fig. 5) and S_4 with $k_0 = 3.94$ (cf. Fig. 6). In this case, the flow regime of the bridge solution W_4^{-5} is no longer periodic in the axial direction as shown in Fig. 9. Instead, the solution has the parallelogram shape periodic cells, which are spanned by Eqs. (9) and (10) (cf. Fig. 1) as indicated by the solid and dashed lines, satisfying relative periodicity in the axial
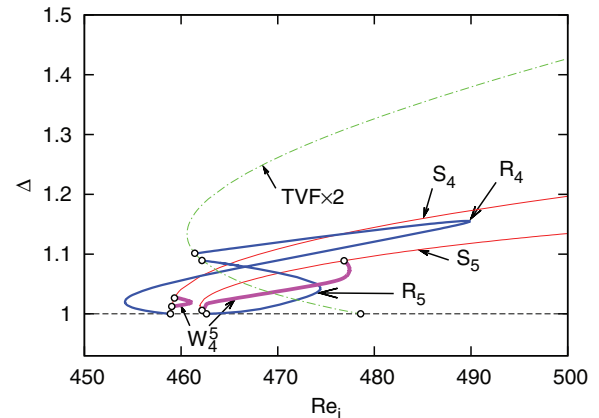

FIG. 5. (Color online) The caption is the same as Fig. 4, except for $k_0^+ < k_0 = 5.125$.

FIG. 6. (Color online) The caption is the same as Fig. 4, except for $k_0^+ > k_0 = 3.94$. The green (light gray) dot-dashed curve is the TVF $\times$ 2 solution branch (cf. Fig. 3).
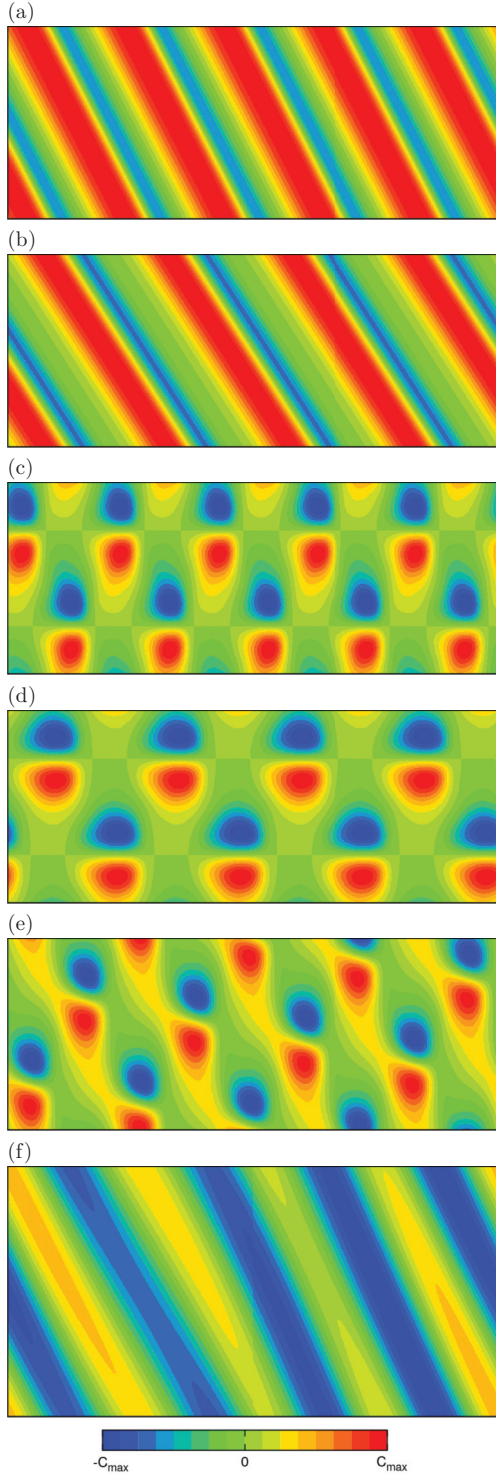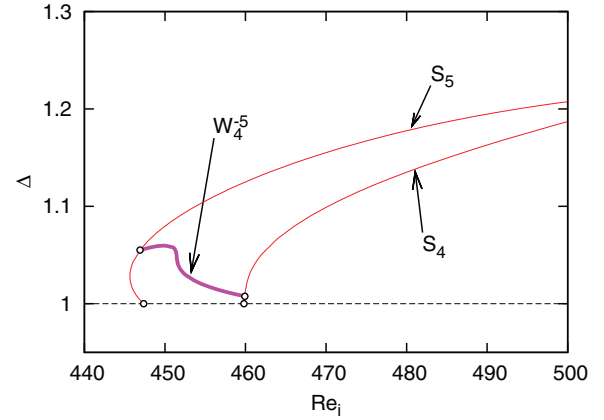
FIG. 8. (Color online) The bifurcation diagram of the WSP type bridge solution W_4^{-5} between the SPI type solution branches for $S_{-5}(k_0 = 5.125)$ and $S_4(k_0 = 3.94)$. The W_4^{-5} solution has phases $[\varphi_1, \varphi_2]$ where the form of phases $\varphi_1 = -5\theta + 5.125z - c_1t$ and $\varphi_2 = 4\theta + 3.94z - c_2t$ is identical to the phase of S^5 and S_{-4}, respectively (note that c_1 and c_2 of the mixed solution differ from those of the original SPI solutions due to nonlinear collections).

direction. Note that the pitches of these lines are identical to those of the S_4 and S_{-5} solutions, respectively.

C. SPI-TVF interactions

As for the SPI-SPI interactions in the last subsection, we can also consider the mixed WSP type solution by the SPI-TVF interaction. In addition, it is possible to compute mixed solutions of two SPI disturbances, which are mirror images, and a TVF disturbance, which is considered to be a RIB-TVF interaction recalling the former pair of SPIs creates a RIB in a special situation: The RIB disturbance has the phases $[\varphi_1, \varphi_2] = [a\theta + bz + ct, -a\theta + bz - ct]$, and the TVF disturbance has the phase $\varphi = Qbz$ where either $Q \in \mathbb{Z}$ or $1/Q \in \mathbb{Z}$ is satisfied. In this case, the superimposed state $\mathbf{X} = \mathbf{X}_R + \tau_{0,\delta}\mathbf{X}_T$, where $\delta \in \mathbb{R}$ is a relative axial shift value between the RIB disturbance $\mathbf{X}_R$ and the TVF disturbance $\mathbf{X}_T$, can be rewritten in a two-phase state as follows.
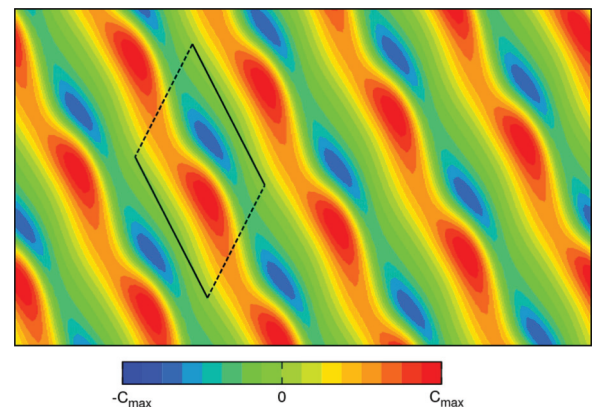

FIG. 9. (Color online) The azimuthal vorticity ω of the W_4^{-5} solution in Fig. 8 for $Re_i = 450$ at $r - r_m = -0.25$ and $(\theta, z) \in [0, 2\pi] \times [0, 3\pi/5.125]$. $C_{max} = 138.43$. The flow is periodic in the parallelogram shape domain bounded by solid and dashed lines spanned by Eqs. (9) and (10) (cf. Fig. 1).

FIG. 7. (Color online) The azimuthal vorticity $\omega = \partial_z u - \partial_r w$ of various flow states as indicated on the unrolled cylinder surface $r - r_m = -0.25$. The horizontal axis represents $\theta \in [0, 2\pi]$, whereas, the vertical axis is $z \in [0, 2\pi/k_0]$ where $k_0 = 5.125$ for (a)–(e), whereas, $k_0 = 3.94$ for (f). The maximum magnitude of ω, denoted as C_{max} in the color bar, are (a) 205.26, (b) 193.60, (c) 200.43, (d) 206.76, (e) 147.74, and (f) 12.93. (a) The S_5 solution in Fig. 5 at $Re_i = 480$. (b) The S_4 solution in Fig. 5 at $Re_i = 480$. (c) The R_5 solution in Fig. 5 at $Re_i = 480$. (d) The R_4 solution in Fig. 5 at $Re_i = 480$. (e) The W_4^{-5} solution in Fig. 5 at $Re_i = 460$. (f) The W_4^5 solution in Fig. 6 at $Re_i = 470$.

(1) For the interaction of the RIB and subharmonic TVF disturbances (the fundamental axial period of the TVF disturbance is shorter than that of the RIB disturbance), i.e., $Q \in \mathbb{Z}$, the proper choice of phases is $(\varphi_1, \varphi_2) = (a\theta + ct, bz)$. Therefore, the superimposed solution must have TWI, WVF, or RIB type symmetry (see Sec. III), i.e., at least one of the reflection and shift-reflection symmetries must be satisfied. Noting that by considering the periodicity of $\mathbf{X}_R$ and $\mathbf{X}_T$,

$$\mathbf{X}_R = \tau_{0,\delta}\mathbf{X}_R \Leftrightarrow \delta \in \mathbb{Z},$$
$$\mathbf{X}_T = \tau_{0,\delta/Q}\mathbf{X}_T \Leftrightarrow \delta \in \mathbb{Z},$$

we can find the following two cases to be allowed.

(i) If $\sigma\mathbf{X}_R = \mathbf{X}_R$ and $\sigma\mathbf{X}_T = \tau_{0,\delta}\sigma\mathbf{X}_T$, the superimposed solution has reflection symmetry. A simple calculation yields that the shift value must be $\delta \in \frac{\mathbb{Z}}{Q}$.

(ii) If $\tau_{0,1/2}\sigma\mathbf{X}_R = \mathbf{X}_R$ and $\tau_{0,1/2}\sigma\mathbf{X}_T = \tau_{0,\delta}\sigma\mathbf{X}_T$, the superimposed solution has shift-reflection symmetry. The shift value must be $\delta \in \frac{\mathbb{Z}+Q/2}{Q}$.

(2) For the interaction of the RIB and superharmonic TVF disturbances (the fundamental axial period of the TVF disturbance is longer than that of the RIB disturbance), i.e., $1/Q \in \mathbb{Z}$, the proper choice of phases is $(\varphi_1, \varphi_2) = (a\theta + ct, Qbz)$. The periodic conditions are

$$\mathbf{X}_R = \tau_{0,Q\delta}\mathbf{X}_R \Leftrightarrow \delta \in \mathbb{Z},$$
$$\mathbf{X}_T = \tau_{0,\delta}\mathbf{X}_T \Leftrightarrow \delta \in \mathbb{Z}.$$

The condition that the superimposed solution must have at least one of the reflection and shift-reflection symmetries yields the following two cases.

(i) If $\sigma\mathbf{X}_R = \mathbf{X}_R$ and $\sigma\mathbf{X}_T = \tau_{0,\delta}\sigma\mathbf{X}_T$, the superimposed solution has reflection symmetry. The shift value must be $\delta \in \mathbb{Z}$.

(ii) If $\tau_{0,Q/2}\sigma\mathbf{X}_R = \mathbf{X}_R$ and $\tau_{0,Q/2}\sigma\mathbf{X}_T = \tau_{0,\delta}\sigma\mathbf{X}_T$, the superimposed solution has shift-reflection symmetry. The shift value must be $\delta \in \mathbb{Z} + Q/2$.

From the above arguments, one finds, if $Q[1/Q]$ is odd, the resultant mixed state has either TWI or WVF type symmetry depending on the choice of shift value δ, whereas, if $Q[1/Q]$ is even, the mixed state always has a RIB type symmetry. In the following, we demonstrate these types of interactions in our numerical code restricting attention to $Q = 1$ (odd case) and $Q = 2$ (even case).

First, we investigate the odd case by examining interactions of the SPI disturbance with $n_0 = \pm 4$ and a TVF disturbance near their bicritical point at $(k_0^\triangle, \mathrm{Re}_i^\triangle) = (9.217, 486.67)$ (cf. Fig. 3). Figures 10(a) and 10(b) represent bifurcation diagrams at $k_0 = 9.16 < k_0^\triangle$ and $k_0 = 9.28 > k_0^\triangle$, respectively. In the figure, the bifurcation point of the TWI (WVF) solution branch makes a transfer from the TVF (RIB) solution branch to the RIB (TVF) solution branch when k_0 crosses $k_0^\triangle$. Also, the bifurcation point of the WSP solution branch moves from the WVF solution branch to the SPI solution branch. These transfers do not change the global picture of the bifurcation diagram shown in Fig. 11.

Figure 12 illustrates the flow fields of the solutions in Fig. 11. These visualizations and the schematics illustrated in Fig. 13 should help readers' intuitive understanding of the interaction. As can be seen in both figures, the axes of reflection symmetry (black solid line in Fig. 13) and
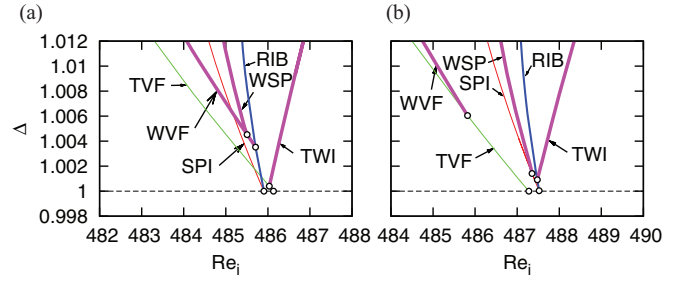

FIG. 10. (Color online) The bifurcation diagrams near the bicritical point of SPI ($n_0 = 4$) and TVF disturbances $(k_0^\triangle, \mathrm{Re}_i^\triangle) = (9.217, 486.67)$ in Fig. 3, for (a) $k_0^\triangle > k_0 = 9.16$ and (b) $k_0^\triangle < k_0 = 9.28$. The green (light gray) thin, red (medium gray) thin, and blue (dark gray) medium thick curves correspond to the solutions with TVF, SPI, and RIB symmetries, respectively. The magenta (medium gray) thick curves are the TWI, WVF, and WSP type mixed solutions.

the axes of shift-reflection symmetry (gray dashed line in Fig. 13) alternately are placed for the RIB disturbance in each quarter axial period, whereas, the symmetry axes where the TVF disturbance satisfies both reflection and shift-reflection symmetries are at each half axial period. Therefore, when we adjust the axial shift value δ to conform to the symmetry axes of the TVF disturbance and the axes of reflection (shift-reflection) symmetry of the RIB disturbance, the superimposed state cannot have shift-reflection (reflection) symmetry. Thus, in general, the interaction of the odd-cell TVF and RIB disturbances results in a TWI or WVF solution.

Interactions of a SPI disturbance with $n_0 = \pm 5$ and a TVF $\times 2$ disturbance are also studied to see an even case scenario in the vicinity of the corresponding bicritical point at $(k_0^\square, \mathrm{Re}_i^\square) = (3.591, 478.21)$ (cf. Fig. 3). The bifurcation diagrams of the RIB solutions at $k_0 = 3.5 < k_0^\square$ and $k_0 = 3.7 > k_0^\square$ are shown in Figs. 14(a) and 14(b), respectively, where each of the RIB solution branches bridges the TVF solution branch and the SPI linear critical point. This fact implies annihilation of the end points of the bridge at the bicritical point, and therefore, these mixed solution branches at $k_0 < k_0^\square$ and $k_0 > k_0^\square$ are considered to belong to distinct solution families. Although both of the mixed solutions have RIB type symmetry and are essentially same as the
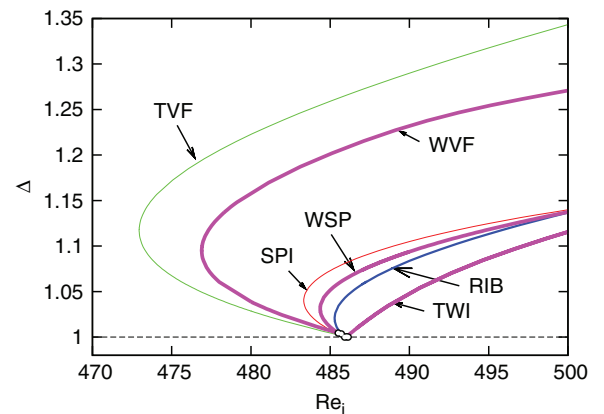

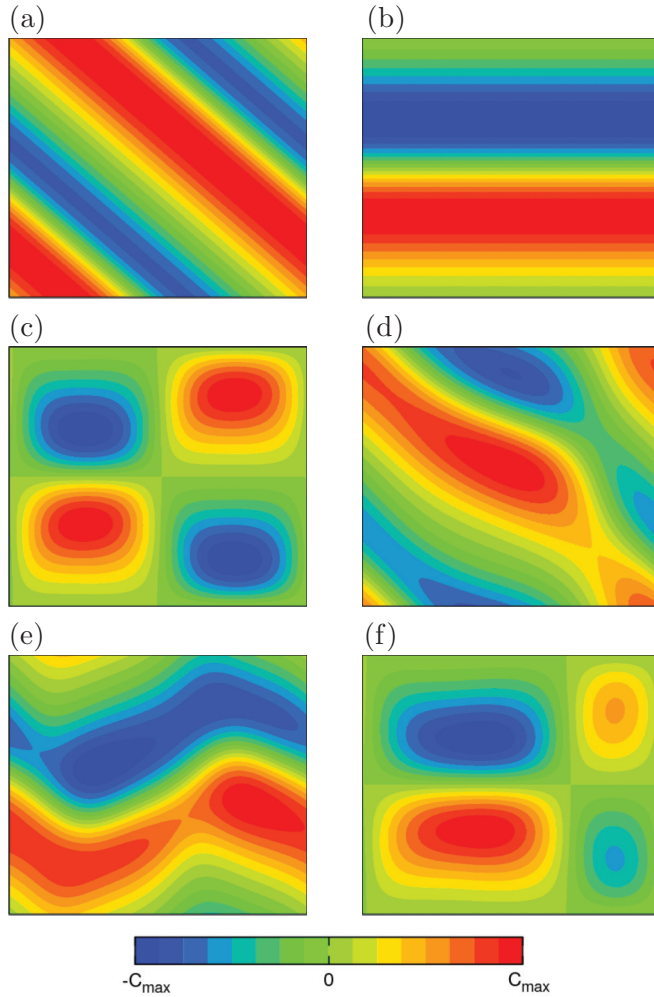FIG. 11. (Color online) The same as in Fig. 10(a) but for a broader range of Re_i.

FIG. 12. (Color online) The azimuthal vorticity ω at $r - r_m = -0.25$ for the different flow states indicated in Fig. 11 at $\mathrm{Re}_i = 490$. The horizontal axis represents $\theta \in [0, 2\pi/4]$, whereas, the vertical axis represents $z \in [0, 2\pi/9.16]$. The values of $C_{\max}$ are (a) 131.75, (b) 189.54, (c) 145.40, (d) 151.66, (e) 211.13, and (f) 113.36. (a) The SPI solution. (b) The TVF solution. (c) The RIB solution. (d) The WSP solution. (e) The WVF solution. (f) The TWI solution.
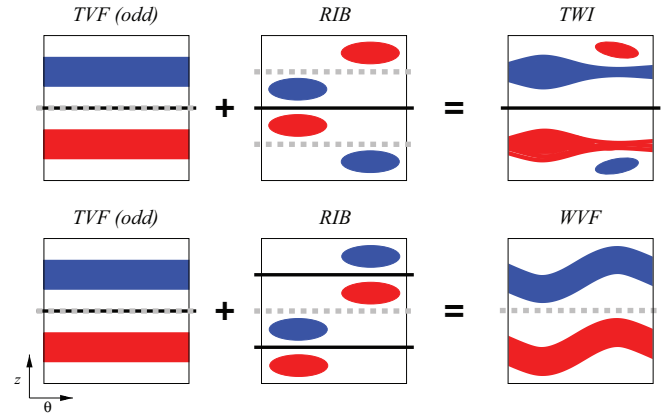

FIG. 13. (Color online) The schematics of the vortex patterns for the interactions of TVF and RIB disturbances in the plane of an unrolled cylinder surface in the annulus. The red (medium gray) and blue (dark gray) colored regions correspond to positive and negative azimuthal vorticity ω, respectively. The squares cover one azimuthal and axial period of the RIB. Horizontal black solid and gray dashed lines characterize the axes of reflection and shift-reflection symmetries, respectively. The interaction of a RIB solution with an odd-cell TVF solution results in either a TWI or a WVF solution. Note that there are also symmetry axes at the axial boundaries of the schematics, although we omit them here and in Fig. 16 for the sake of visibility.

D. TVF-TVF interactions

In this subsection, which concerns the interactions of two TVF disturbances, all of the solutions are axisymmetric and, therefore, invariant in the azimuthal direction. The two linear critical curves of the TVF instabilities, for which seven and eight cells exist in $z \in [0, 2\pi/k_0]$, are shown in Fig. 17. The bicritical point of these instabilities is at $(k_0, \mathrm{Re}_i) = (0.99, 478.73)$.

By choosing $k_0 = 0.96$, we superimpose these TVF disturbances. Note that the mixed solution, which has phases $[\varphi_1, \varphi_2] = [7k_0z, 8k_0z]$, can be written in a function of only one phase $\varphi = k_0z$ (see Sec. III B). Figure 18(a) illustrates the resultant mixed solution branch [thick magenta (medium gray) curves labeled as (mixed) TVF], which bridges the pure seven- and eight-cell TVF solution branches [thin green (light
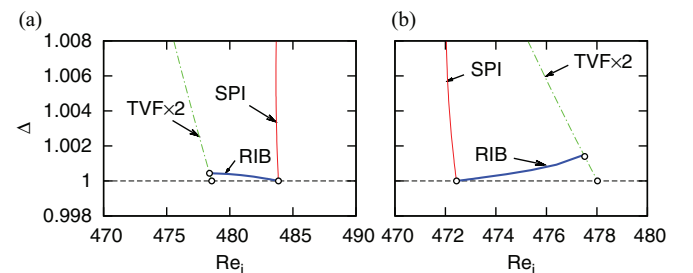
RIB solutions arising from the interaction of the two SPI linear critical modes being mirror images, their typical flow characteristics are of interest.

As shown in the schematics (Fig. 16), symmetry axes of the TVF × 2 disturbances are at the inflow boundaries (negative vorticity at the upper side and positive vorticity at the lower side) and the outflow boundaries (positive vorticity at the upper side and negative vorticity at the lower side). When a TVF × 2 solution is perturbed by a RIB disturbance so that the shift-reflection symmetry axes at the inflow boundaries of the TVF × 2 solution are preserved, one observes the so-called wavy-inflow-boundary-like structure [Figs. 15(a) and 16 (top)]. Similarly, when the outflow boundaries of a TVF × 2 solution and the shift-reflection symmetry axes of a RIB disturbance coincide, the wavy-outflow-boundary-like structure emerges [Figs. 15(b) and 16 (bottom)].

FIG. 14. (Color online) The bifurcation diagrams near the bicritical point of SPI ($n_0 = 5$) and TVF × 2 disturbances $(k_0^\square, \mathrm{Re}_i^\square) = (3.591, 478.21)$ in Fig. 3 for (a) $k_0 = 3.5$ and (b) $k_0 = 3.7$. The dot-dashed green (light gray) thin curve represents the TVF × 2 solution, whereas, the solid red (medium gray) thin and blue (dark gray) medium thick curves correspond to the solutions with SPI and RIB symmetries, respectively.
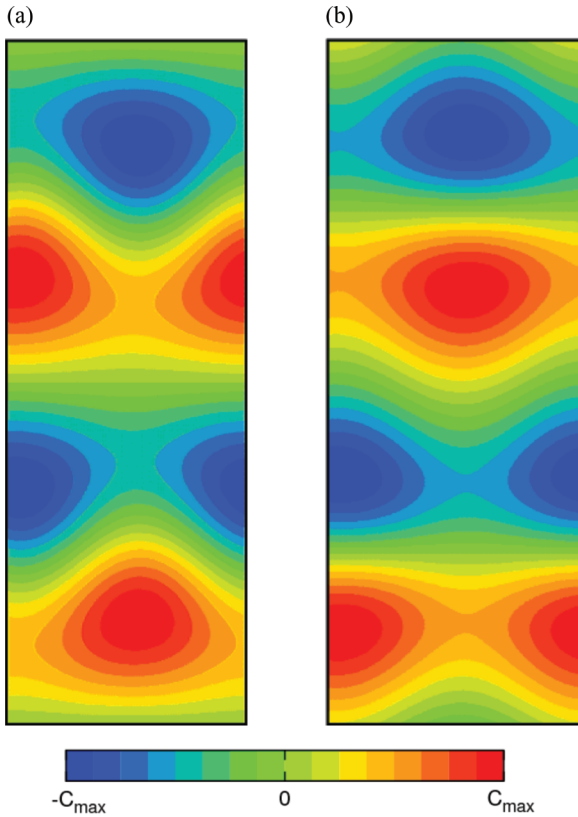
FIG. 15. (Color online) The azimuthal vorticity ω at $r - r_m = -0.25$ for the RIB solutions in Fig. 14. (a) $(k_0, \mathrm{Re}_i) = (3.5, 478.5)$ (seems like a wavy inflow boundary) and (b) $(k_0, \mathrm{Re}_i) = (3.7, 477.4)$ (seems like a wavy outflow boundary). The horizontal axis represents $\theta \in [0, 2\pi/5]$, whereas, the vertical axis represents $z \in [0, 2\pi/k_0]$. The values of $C_{\max}$ are 17.91 for (a) and 12.93 for (b).

gray) curves labeled TVF $\times$ 7 and TVF $\times$ 8, respectively]. Figures 19(a)–19(c) show the flow regimes of these solutions at $\mathrm{Re}_i = 476$. Although the mixed solution that has fundamental periodicity $z \in [0, 2\pi/k_0]$ also has TVF symmetry, the corresponding vortex structure is now modulated and has a
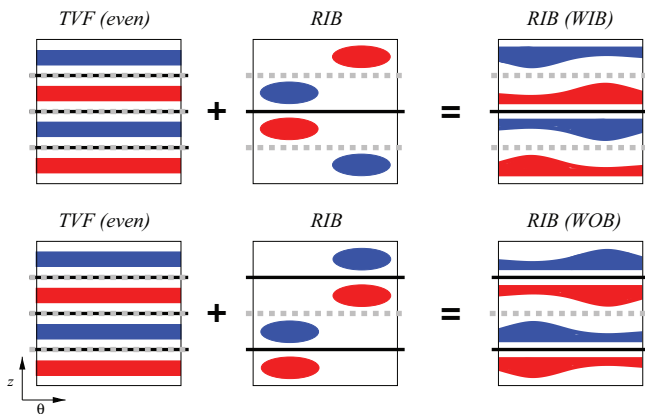

FIG. 16. (Color online) The same as in Fig. 13 but for interactions of TVF $\times$ 2 and RIB disturbances. Although both of the superimposed states in the top and bottom figures for the different axial shift value δ result in RIB symmetry, again, their vortex structures show distinct WIB- and WOB-like patterns, respectively.
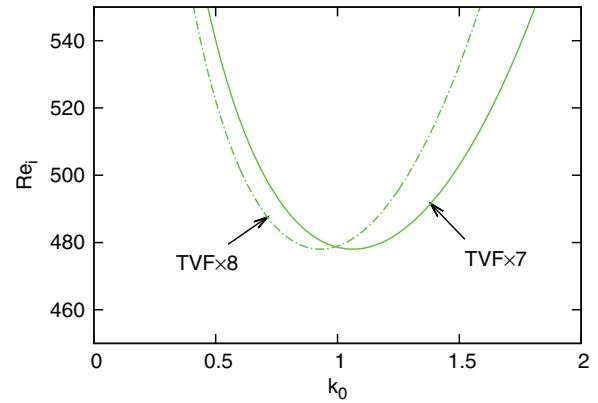

FIG. 17. (Color online) Solid curve: The linear critical curves of TVF $\times$ 7 and dot-dashed curve: TVF $\times$ 8 instabilities against k_0. The crossing point of these curves is at $(k_0, \mathrm{Re}_i) = (0.99, 478.73)$.

fringe-shift-like appearance due to the interference of the pure cell states. A similar bifurcation scenario has been investigated, for example, in Ref. [24].

Our numerical method also allows us to consider the generalized interaction analysis for TVF disturbances with irrational wave numbers. Figure 18(b) shows the bifurcation
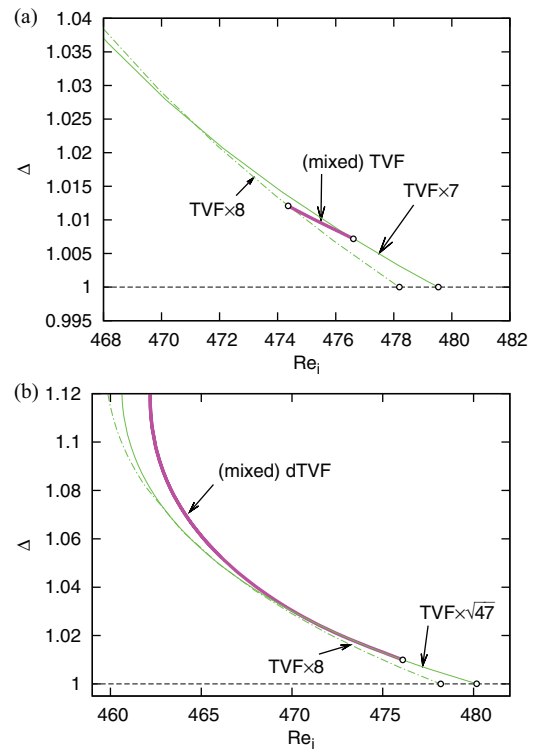

FIG. 18. (Color online) The bifurcation diagrams for $k_0 = 0.96$. The thin green (light gray) curves represent the pure TVF solutions. Note that the thin solid and dot-dashed green (light gray) curves in (a), which represent TVF $\times$ 7 and TVF $\times$ 8 solution branches, respectively, bifurcate from the corresponding critical curves in Fig. 17. The mixed solutions between rational and irrational wave number TVF solutions are indicated by magenta (medium gray) thick curves in (a) and (b), respectively. Note that the mixed TVF solution in (a) has phases $[\varphi_1, \varphi_2] = [7k_0 z, 8k_0 z]$, whereas, the dTVF solution in (b) has phases $[\varphi_1, \varphi_2] = [7k_0 z, \sqrt{47}k_0 z]$.
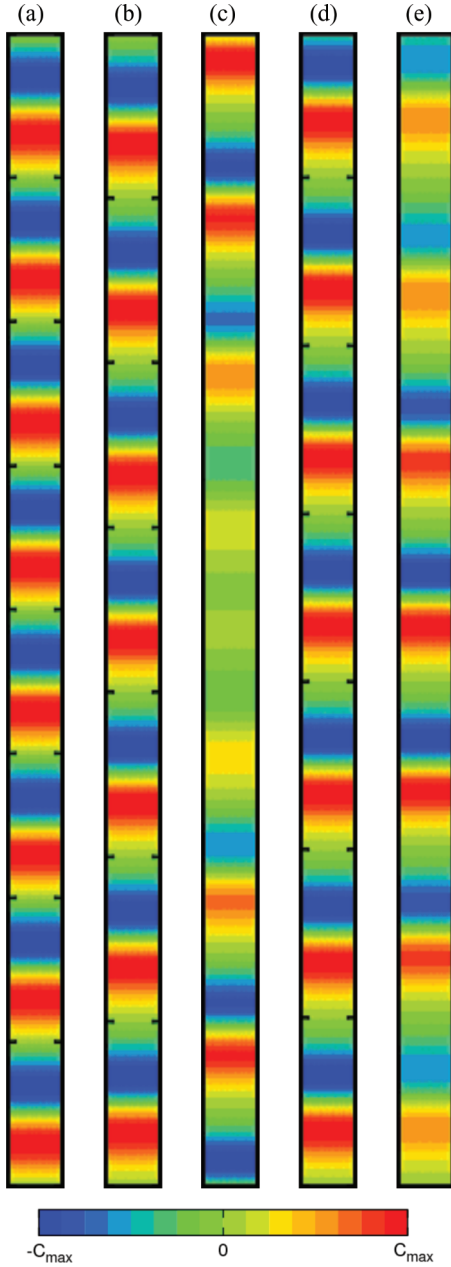
FIG. 19. (Color online) The azimuthal vorticity ω at $r - r_m = -0.25, (\theta, z) \in [0, 2\pi/10] \times [0, 2\pi/0.96]$, and $Re_i = 476$ for the solutions shown in Fig. 18. (a)–(c) correspond to the TVF × 8, TVF × 7, and mixed TVF solutions in Fig. 18(a), respectively, whereas, (d) and (e) correspond to the TVF × $\sqrt{47}$ and mixed dTVF solutions in Fig. 18(b), respectively. The symmetry axes of the solutions are adjusted at $z = 0$ (bottom of the pictures). The values of C_{max} are (a) 18.42, (b) 23.05, (c) 32.58, (d) 12.89, and (e) 31.41. The tics in (a), (b), and (d) represent the fundamental period of corresponding solutions $2\pi/(8 \times 0.96), 2\pi/(7 \times 0.96)$, and $2\pi/(\sqrt{47} \times 0.96)$, respectively. Obviously, the (c) mixed TVF and (e) mixed dTVF have no smaller fundamental subdivisions.

diagram where the wave number of the seven-cell TVF solution of Fig. 18(a) is slightly changed to a $\sqrt{47}$ cell state, i.e., the solid curve of Fig. 18(b) represents the TVF × $\sqrt{47}$ solution branch. As its visualization, Fig. 19(d) shows there exist six cells and an additional incomplete cell in $z \in [0, 2\pi/k_0]$. The
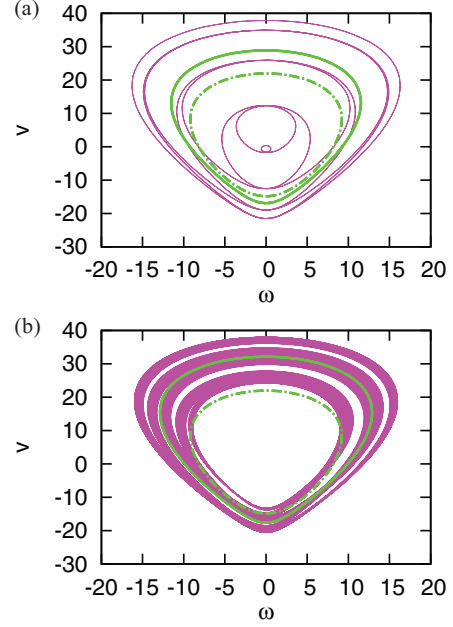

FIG. 20. (Color online) The phase portrait of azimuthal velocity v and vorticity ω. The radial position is at $r - r_m = -0.25$, and the range of z is $[0, 40 \times 2\pi/0.96]$. Although the thicknesses of the curves are replaced for the sake of visibility, the curves in (a) and (b) correspond to the solutions in Figs. 18(a) and 18(b), respectively. Therefore, in (a) [(b)], the thick solid and dot-dashed green (light gray) curves indicate TVF × 7 (TVF × $\sqrt{47}$) and TVF × 8 solutions, respectively, whereas, the magenta (medium gray) curve illustrates the mixed TVF (dTVF) solution.

bifurcation diagram also shows the detachment of the mixed solution branch [labeled as (mixed) dTVF], which has phases $[\varphi_1, \varphi_2] = [7k_0z, \sqrt{47}k_0z]$ from the TVF × 8 solution branch. This mixed solution essentially has dTVF symmetry because there is no reduction to a one-phase TVF state in contrast to the rational wave number case. Indeed, as shown in Fig. 19(e), the flow field of the mixed solution is no longer periodic in $z \in [0, 2\pi/k_0]$ because of the double periodicity of the dTVF symmetry.

In order to see this particular spatial structure of the solution more clearly, the azimuthal velocity v and vorticity ω are combined in Fig. 20 where the axial range is extended to $z \in [0, 40 \times 2\pi/k_0]$. For the pure TVF solutions, drawn by the green (light gray) curves, a pair of vortices forms a round of the curve in the figure. In contrast, for the former mixed TVF solution presented in Fig. 18(a), the corresponding magenta (medium gray) curve forms a closed loop structure with several rounds [cf. Fig. 20(a)], whereas, for the latter mixed dTVF solution presented in Fig. 18(b), the corresponding spiraling curve never returns to its starting point, finally filling the whole torus projected in the (v, ω) space [cf. Fig. 20(b)].

V. CONCLUSIONS AND DISCUSSIONS

In this paper, we elucidated the interactions of various TVF and SPI solutions of Taylor-Couette flow with different azimuthal and axial wave numbers. The bifurcation curves of mixed solutions are captured by our Newton solver, which can compute any solution with up to two phases, using

superimposed linear critical solutions as an initial guess in the vicinity of the bicritical points. We considered rational and irrational axial wave numbers of interacting contributions to the mixed state providing a theoretical discussion for the classification of resultant solutions. The obtained mixed solution branches, which result in sub- or supercritical secondary bifurcation or footbridge solutions, continue to exist beyond the weakly nonlinear parameter ranges.

When linear critical curves of two SPI modes with different azimuthal wave numbers intersect at a particular parameter choice, there exist four linear critical SPI modes, i.e., a pair of degenerate left- and right-winding SPI solutions for each SPI linear instability. Restricting attention to the interactions of two SPI modes, we obtained all six possible combinations of them. These mixed solutions result in two RIB solutions and two WSP solution pairs, each of which are degenerate in the bifurcation diagram. The WSP solutions include the superpositions of the SPI modes with equal signs of helicity, which is reported here. When the interaction happens between SPI solutions with the irrational wave number case, a parallelogram shape calculation domain is used to describe the resultant spiral dominated pattern with relative axial periodicity.

We calculated various interactions between SPI and TVF modes as the SPI-SPI interaction case. In this case, we found it is possible to calculate a RIB-TVF interaction, which is a special case of the SPI-SPI-TVF interaction. The symmetries of the resultant mixed solutions depend on whether the ratio of axial wave numbers of the RIB and TVF is an odd or even integer.

At the bicritical point, we have confirmed WVF and TWI type solutions bifurcate for the odd case, whereas, two RIB type solutions, which have WIB- and WOB-like structures, bifurcate for the even case. These scenarios are consistent with those which have been described in weakly nonlinear theory at the TVF-SPI bicritical point [2–6]. By using schematics of the superpositions of the RIB and TVF modes, comprehensive explanations are given for these interactions.

We also investigated TVF-TVF interactions, wherein, axially inhomogeneous Taylor vortex patterns are observed. Our approach allows us to calculate spatially doubly periodic solutions which arise from an interaction between two TVF solutions having irrational wave numbers.

All of the investigations above prove our phase symmetry analysis, and the Newton solver helps to obtain finite-amplitude solutions whose flow patterns are of interest. This strategy is sometimes useful for providing a comprehensive physical explanation for the structure of the complicated mixed solution when its connection to linear instability is revealed. As an example, we reproduce the SPI and RIB type low axial wave number solutions discovered in Ref. [20] in our code as in Fig. 21. Although they failed to trace their RIB type low axial wave number solution branch for relatively small Re_i, we can complete the bifurcation scenario with our code. As can be seen in the figure, we understand this solution is originated from the interaction of TVF × 2 and TVF × 4, respectively, and SPI (azimuthal wave number $n_0 = 3$), which are almost bicritical in this axial wave number choice.

Our strategy provides a systematic approach to create solutions with axially large scale structures, which would be responsible for sustaining the large scale spiral
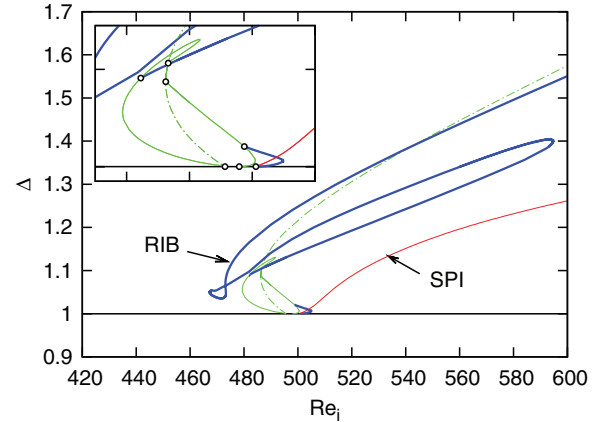

FIG. 21. (Color online) The variation in CCF-normalized torque Δ for various solutions at $(\eta, Re_o, k_0) = (0.883, -1200, 2.5)$. The low axial wave number SPI ($n_0 = 3$) and RIB ($n_0 = 3$) solutions in Ref. [20] are drawn by thin solid red (medium gray) and thick solid blue (dark gray) curves, respectively, with arrow indications. The small segment of thick blue (dark gray) curve bifurcated from the CCF, black line at $\Delta = 1$, is also a RIB type solution. The solid and dot-dashed green (light gray) curves represent the TVF × 2 and TVF × 4 solutions. The open circles in the enlarged picture indicate bifurcation points and are omitted in the main figure for the sake of visibility. There are three linear critical points of the CCF, which correspond to TVF × 4, TVF × 2, and SPI ($n_0 = \pm 3$) from left to right. After the TVF × 4 solution branch is bifurcated from the CCF, the bifurcation of the TVF × 2 solution branch arises very soon from the TVF × 4 solution branch, and thus, we cannot separate these bifurcation points in the present scale.

turbulence [15–19]. In these experimental and numerical results, the observed pattern has a chaotic motion rather than an equilibrated state. Thus, borrowing the idea of dynamical systems theory applied in the shear-flow transition problem, our solutions, most of which may be unstable, are likely to form the "backbone" of this dynamics.

We can compare our solutions and simulation results with Ref. [18] for $R_o = -1200$. When R_i is slightly above the relaminarization threshold, a modulated spiral pattern, called interpenetrating spirals, can be found. Some of the transient and spatially local elements of the modulated pattern resemble the two-phase solutions we investigated. As increasing R_i, the flow regime evolves into a striping large scale laminar-turbulent structure. The nonlinear fringe-shift, which will become more evident with the further introduction of mode interactions, is considered to be one of the possible physical explanations to emerge from this laminar-turbulent coexisting pattern. Another feature of the spiral turbulence is that it is triggered by subcritical transition for higher $|R_o|$. Although the mixed solutions presented in this paper are mostly settled within the linear unstable parameter region, one can expect that solutions with higher $|R_o|$ and larger structures emerge in a highly subcritical manner. The axial relative periodicity would help this investigation as we illustrated in Sec. I.

There would also be some connections to the similar turbulent stripe simulation of the plane Couette flow in the tilted rectangular domain in Ref. [25]. Further work might be

able to continue the finite-amplitude solution branches of the plane Couette flow discovered in the rectangular domain (e.g., Ref. [9]) for the tilted rectangular domain. Recently, it has been found that spanwise (axial) mean flow is indispensable to stripe turbulence [26]. Even when the starting solution in the rectangular domain does not have spanwise mean flow due to axial symmetry, the continuation for the tilted rectangular domain breaks the symmetry, and therefore, spanwise mean flow must be produced. We would be able to introduce modulation to the solution in the tilted domain by seeking the bifurcating solution branch, via Floquet stability analysis, to this subspace.

Finally, we remark that the phase symmetry analysis introduced in Sec. III can be applicable to bifurcations of more than three-phase mixed states where, typically, phase dependence cannot be accommodated in two spatial periodic directions, and, thus, there is a time-dependent pattern in the sense of the spatially averaged field. Our restriction up to two phases can be removed when we switch to a more advanced numerical strategy, e.g., the Newton-Krylov approach [27,28]. Returning to the Taylor-Couette flow problem, such time-dependent coherent patterns have been observed in experiments and simulations [8,29,30]. More than three-phase solutions, bifurcating from the bicritical points, which are sometimes predicted in weakly nonlinear theory, are likely to elucidate these complex pattern formation phenomena.

ACKNOWLEDGMENT

[1] C. D. Andereck, S. S. Liu, and H. L. Swinney, J. Fluid Mech. **164**, 155 (1986).

[2] A. Davey, R. C. DiPrima, and J. T. Stuart, J. Fluid Mech. **31**, 17 (1968).

[3] G. Iooss, J. Fluid Mech. **173**, 273 (1986).

[4] M. Golubitsky, I. Stewart, and D. G. Schaeffer, in *Singularities and Groups in Bifurcation Theory*, Springer Series in Applied Mathematical Sciences 69, Vol. II (Springer, New York, 1988).

[5] M. Golubitsky and W. F. Langford, Physica D **32**, 362 (1988).

[6] P. Chossat and G. Iooss, in *The Couette-Taylor Problem*, Springer Series in Applied Mathematical Sciences 102 (Springer, New York, 1994).

[7] J. J. Hegseth, G. W. Baxter, and C. D. Andereck, Phys. Rev. E **53**, 507 (1996).

[8] C. D. Andereck, R. Dickman, and H. L. Swinney, Phys. Fluids **26**, 1395 (1983).

[9] M. Nagata, J. Fluid Mech. **188**, 585 (1988).

[10] E. Weisshaar, F. H. Busse, and M. Nagata, J. Fluid Mech. **226**, 549 (1991).

[11] R. Tagg, W. S. Edwards, H. L. Swinney, and P. S. Marcus, Phys. Rev. A **39**, 3734 (1989).

[12] A. Pinter, M. Lücke, and C. Hoffmann, Phys. Rev. Lett. **96**, 044506 (2006).

[13] S. Altmeyer and C. Hoffmann, New J. Phys. **12**, 113035 (2010).

[14] C. Hoffmann, S. Altmeyer, A. Pinter, and M. Lücke, New J. Phys. **11**, 053002 (2009).

[15] D. Coles, J. Fluid Mech. **21**, 385 (1965).

[16] C. van Atta, J. Fluid Mech. **25**, 495 (1966).

[17] A. Prigent, G. Grégoire, H. Chaté, O. Dauchot, and W. van Saarloos, Phys. Rev. Lett. **89**, 014501 (2002).

[18] A. Meseguer, F. Mellibovsky, M. Avila, and F. Marques, Phys. Rev. E **80**, 046315 (2009).

[19] M. J. Burin and C. J. Czarnocki, J. Fluid Mech. **709**, 106 (2012).

[20] A. Meseguer, F. Mellibovsky, M. Avila, and F. Marques, Phys. Rev. E **79**, 036309 (2009).

[21] K. Deguchi and M. Nagata, J. Fluid Mech. **678**, 156 (2011).

[22] F. Marques, Phys. Fluids A **2**, 729 (1990).

[23] I. Soibelman and D. L. Meiron, J. Fluid Mech. **229**, 389 (1991).

[24] R. Meyer-Spasche and H. B. Keller, Phys. Fluids **28**, 1248 (1985).

[25] L. S. Tuckerman and D. Barkley, Phys. Fluids **23**, 041301 (2011).

[26] Y. Duguet and P. Schlatter, Phys. Rev. Lett. **110**, 034502 (2013).

[27] J. Sánchez, M. Net, B. García-Archilla, and C. Simó, J. Comput. Phys. **201**, 13 (2004).

[28] D. Viswanath, J. Fluid Mech. **580**, 339 (2007).

[29] P. R. Fenstermacher, H. L. Swinney, and J. P. Gollub, J. Fluid Mech. **94**, 103 (1979).

[30] K. T. Coughlin, P. S. Marcus, R. P. Tagg, and H. L. Swinney, Phys. Rev. Lett. **66**, 1161 (1991).